

Article

# Sequential Synthesis Methodology Yielding Well-Defined Porous 75% SrTiO<sub>3</sub>/25% NiFe<sub>2</sub>O<sub>4</sub> Nanocomposite

Ilyes Baba-Ahmed <sup>1</sup>, Daniel Ghercă <sup>2,†</sup>, Alexandra-Raluca Iordan <sup>3</sup>, Mircea Nicolae Palamaru <sup>3</sup>, Carmen Mita <sup>3</sup>, Rachid Baghdad <sup>4</sup>, Gabriel Ababei <sup>2</sup> , Nicoleta Lupu <sup>2</sup> , Mohamed Amine Benamar <sup>5</sup> , Abdelkader Abderrahmane <sup>6</sup>, Tiberiu Roman <sup>7</sup>, Georgiana Bulai <sup>7</sup> , Liviu Leontie <sup>8</sup>  and Adrian Iulian Borhan <sup>2,3,\*,†</sup>

- <sup>1</sup> Laboratory of Fundamental and Applied Physics (FUNDAPL), Physics Department, Sciences Faculty, Saad Dahleb Blida 1 University, BP 270, Blida 09000, Algeria; baba.ing.ebm@gmail.com
- <sup>2</sup> National Institute of Research and Development for Technical Physics, 47 Mangeron Boulevard, 700050 Iasi, Romania; dgherca@phys-iasi.ro (D.G.); gababei@phys-iasi.ro (G.A.); nicole@phys-iasi.ro (N.L.)
- <sup>3</sup> Faculty of Chemistry, Alexandru Ioan Cuza University of Iasi, 11 Carol I Boulevard, 700506 Iasi, Romania; alexandra.iordan@uaic.ro (A.-R.I.); palamaru@uaic.ro (M.N.P.); cmita@uaic.ro (C.M.)
- <sup>4</sup> Synthesis and Catalysis Laboratory, Matter Sciences Faculty, Ibn Khaldoun University of Tiaret, Tiaret 14000, Algeria; baghdadrachid@gmail.com
- <sup>5</sup> Laboratory of Fundamental and Applied Physics (FUNDAPL), University Center of Tamenghasset, Amine Elokkel Elhadj Moussa Eg-Akhamouk, BP 10034, Sersouf, Tamanghasset 11000, Algeria; benamardz64dz@yahoo.fr
- <sup>6</sup> Department of Electrical Engineering, Chosun University, 375, Seosuk-dong, Dong-gu, Gwangju 501759, Korea; abderrahmane.abdelkader@gmail.com
- <sup>7</sup> Integrated Center of Environmental Science Studies in the North-Eastern Development Region (CERNESIM), Department of Exact and Natural Sciences, Institute of Interdisciplinary Research, Alexandru Ioan Cuza University of Iasi, 700506 Iasi, Romania; tiberiu.roman@chem.uaic.ro (T.R.); georgiana.bulai@uaic.ro (G.B.)
- <sup>8</sup> Faculty of Physics, Alexandru Ioan Cuza University of Iasi, 11 Carol I Boulevard, 700506 Iasi, Romania; lleontie@uaic.ro
- \* Correspondence: adrian.borhan@uaic.ro
- † These authors contributed equally to this work.



**Citation:** Baba-Ahmed, I.; Ghercă, D.; Iordan, A.-R.; Palamaru, M.N.; Mita, C.; Baghdad, R.; Ababei, G.; Lupu, N.; Benamar, M.A.; Abderrahmane, A.; et al. Sequential Synthesis Methodology Yielding Well-Defined Porous 75% SrTiO<sub>3</sub>/25% NiFe<sub>2</sub>O<sub>4</sub> Nanocomposite. *Nanomaterials* **2022**, *12*, 138. <https://doi.org/10.3390/nano12010138>

Academic Editor: Yun-Mo Sung

Received: 9 December 2021

Accepted: 28 December 2021

Published: 31 December 2021

**Publisher's Note:** MDPI stays neutral with regard to jurisdictional claims in published maps and institutional affiliations.



**Copyright:** © 2021 by the authors. Licensee MDPI, Basel, Switzerland. This article is an open access article distributed under the terms and conditions of the Creative Commons Attribution (CC BY) license (<https://creativecommons.org/licenses/by/4.0/>).

**Abstract:** In this research, we reported on the formation of highly porous foam SrTiO<sub>3</sub>/NiFe<sub>2</sub>O<sub>4</sub> (100-xSTO/xNFO) heterostructure by joint solid-state and sol-gel auto-combustion techniques. The colloidal assembly process is discussed based on the weight ratio x (x = 0, 25, 50, 75, and 100 wt %) of NiFe<sub>2</sub>O<sub>4</sub> in the 100-xSTO/xNFO system. We proposed a mechanism describing the highly porous framework formation involving the self-assembly of SrTiO<sub>3</sub> due to the gelation process of the nickel ferrite. We used a series of spectrophotometric techniques, including powder X-ray diffraction (XRD), field emission scanning electron microscopy (FESEM), transmission electron microscopy (TEM), N<sub>2</sub> adsorption isotherms method, UV-visible diffuse reflectance spectra (UV-Vis DRS), vibrating sample magnetometer (VSM), and dielectric measurements, to investigate the structural, morphological, optical, magnetic, and dielectric properties of the synthesized samples. As revealed by FE-SEM analysis and textural characteristics, SrTiO<sub>3</sub>-NiFe<sub>2</sub>O<sub>4</sub> nanocomposite self-assembled into a porous foam with an internally well-defined porous structure. HRTEM characterization certifies the distinctive crystalline phases obtained and reveals that SrTiO<sub>3</sub> and NiFe<sub>2</sub>O<sub>4</sub> nanoparticles were closely connected. The specific magnetization, coercivity, and permittivity values are higher in the 75STO/25NFO heterostructure and do not decrease proportionally to the amount of non-magnetic SrTiO<sub>3</sub> present in the composition of samples.

**Keywords:** heterostructure; nanocomposite; porous foam SrTiO<sub>3</sub>/NiFe<sub>2</sub>O<sub>4</sub>; solid-state reaction; sol-gel auto-combustion

## 1. Introduction

Nanomaterials such as nanoparticles, nanowires, nanotubes, nanorods, and quantum dots present unique optoelectronic, electrical, magnetic, and mechanical properties [1]. The development of new strategies to assemble these nanomaterials into patterned heterostructures with multiple functionalities and tailored physical properties is an urgent need for application in nanotechnological devices. The heterostructures offer attractive new possibilities for device applications due to the controlled integration of complementary nanocomponents, which exhibit synergistic effects that combine multiple functionalities in one structure [2,3]. The rapid advances in materials synthesis methods have made it possible to synthesize nanomaterials with well-defined sizes, shapes, structures, and morphologies. Although many heterostructure [4,5] systems have been reported, very few articles have shown the effect of morphology on the physical parameters [6]. Zheng et al. [1] explain that the assembling process of nanomaterials “is critically dependent on the nanostructure morphologies including domain patterns and shapes as well as structures and properties of the interfaces”. Starting from this concept, we present, in this study, how the colloidal assembly of NiFe<sub>2</sub>O<sub>4</sub> nanoparticles can induce structural and morphological changes in a SrTiO<sub>3</sub> matrix, that presents a superposition of cubic and tetragonal phases, depending on the weight ratio  $x$  of NiFe<sub>2</sub>O<sub>4</sub>. Moreover, the colloidal assembly of the attachment of the NiFe<sub>2</sub>O<sub>4</sub> particles in the presence of seed SrTiO<sub>3</sub> particles by using the sol-gel auto-combustion method leads to an open and porous foam morphology. The system SrTiO<sub>3</sub>/NiFe<sub>2</sub>O<sub>4</sub> is known mostly for its capability as a visible-light-driven photocatalyst [7,8]. SrTiO<sub>3</sub> (STO) is a prototypical cubic perovskite oxide with unique physical properties, such as wide bandgap, high dielectric constant, thermal stability, and large permittivity [9–11]. Besides, SrTiO<sub>3</sub> is known as versatile powder support for the formation of heterostructures with specific properties for technological applications [12–16], because SrTiO<sub>3</sub>, as an intrinsic paraelectric, is able to stabilize ferroelectric order via substrate-induced strain, cation doping, <sup>18</sup>O isotope substitutions, and defect engineering [17]. Hence, to induce ferromagnetic properties into SrTiO<sub>3</sub>, some researchers reported doping of STO using iron (Fe) [18], cobalt (Co) [19], manganese (Mn) [11] or by using non-magnetic sp-additives [12]. Recently, a ceramic composite of STO and nickel ferrite NiFe<sub>2</sub>O<sub>4</sub> (NFO) has been reported to show ferroelectric, ferromagnetic, and magneto-dielectric properties [13]. NFO is a well-known nanomaterial with high Curie temperature, high chemical, and structural stability [14], having useful magnetic and electrical properties [8]. NFO is used in a wide range of applications including, electrical memory and switching devices [15], high-performance lithium-ion batteries [16], photocatalysis [20], and cancer therapy [21–23]. On the other hand, porous materials [24,25] have been obtained in the past decade [26,27] by various methods such as self-assembly of primary nanoparticles [28], combustion [29,30], smelting reaction [31], hydrothermal [32]. According to the literature [33], we tried here to extend the sol-gel auto-combustion method for the synthesis of porous heterostructure foams due to the possibility of controlling the chemical composition, homogeneity, morphology, shape, and phase composition of the materials. Unique and interesting features of SrTiO<sub>3</sub>/NiFe<sub>2</sub>O<sub>4</sub> binary composite have gained currently great attention from many research studies [8,34]. Yongmei Xia et al. [34] showed from TEM images of SrTiO<sub>3</sub>/NiFe<sub>2</sub>O<sub>4</sub> nanocomposites, that NiFe<sub>2</sub>O<sub>4</sub> particles are uniformly dispersed onto the SrTiO<sub>3</sub> without any accumulation, proving that the prepared nanocomposite is a uniform mixture of SrTiO<sub>3</sub> and NiFe<sub>2</sub>O<sub>4</sub> nanoparticles [34]. Moreover, in order to obtain hierarchical SrTiO<sub>3</sub>/NiFe<sub>2</sub>O<sub>4</sub> composite nanostructures with an excellent light response, Panpan Jing et al. [8] used single-spinneret electrospinning and a side-by-side-spinneret electrospinning technique. In fact, the main advantage of these techniques is high productivity, but the formation of an uneven distribution of fiber diameter is difficult to avoid, while in the present study the uniformity of such nanocomposite is considered beneficial for our experimental ability to design useful photocatalytic properties in a rational way.

The results presented in this work aim to highlight a new topic and findings on the formation of the porous foam SrTiO<sub>3</sub>/NiFe<sub>2</sub>O<sub>4</sub> (namely  $100-x$ STO/ $x$ NFO), heterostructure

by joint solid-state reaction and sol-gel auto-combustion technique. The mechanism of colloidal assembly is discussed in the present study based on the weight ratio  $x$  ( $x = 0, 25, 50, 75,$  and  $100$  wt %) of  $\text{NiFe}_2\text{O}_4$  in the  $100-x\text{STO}/x\text{NFO}$  system. The rational synthesis presented in this study, with emphasis on the colloidal assembly of the attachment of the  $\text{NiFe}_2\text{O}_4$  particles in the presence of  $\text{SrTiO}_3$ , represents a step forward in reaching multifunctional properties. These advances are at the core of progress in photocatalytic applications, including water remediation (dyes and pharmaceutical drugs degradation) and especially in water splitting (photocatalytic generation of  $\text{H}_2$ ). Thus, synthesized porous  $75\%\text{SrTiO}_3/25\%\text{NiFe}_2\text{O}_4$  nanocomposite materials offer flexibility for integrating multiple functionalities such as catalytic activity, adsorption capacity, photocatalytic activity, and magnetic properties that make them attractive for applications in photocatalysis.

## 2. Materials and Methods

### 2.1. Porous Heterostructure Foams $100-x\text{STO}/x\text{NFO}$ Multistep Synthesis Method

Analytical grade precursors have been used to synthesize our materials, such as strontium carbonate ( $\text{SrCO}_3$ , 99%, UCB chemicals; Brussels, Belgium), titanium dioxide ( $\text{TiO}_2$ , 99%, Loba Feinchemie; Fischamend, Austria), nickel (II) nitrate ( $\text{Ni}(\text{NO}_3)_2 \cdot 6\text{H}_2\text{O}$ , 97%, Sigma Aldrich; Steinheim am Albuch, Baden-Württemberg, Germany), iron (III) nitrate ( $\text{Fe}(\text{NO}_3)_3 \cdot 9\text{H}_2\text{O}$ , 98%] Sigma Aldrich; Steinheim am Albuch, Baden-Württemberg, Germany), glycine ( $\text{NH}_2\text{CH}_2\text{COOH}$ , 99.7%, Merck; Steinheim am Albuch, Baden-Württemberg, Germany). First, the solid-state technique was used for the fabrication of the pristine  $\text{SrTiO}_3$  (STO) nanoparticles by mixing strontium carbonate and titanium dioxide with a molar ratio of 1:1. To ensure high homogeneity, the mixture was ground in an agate mortar for 6 h after adding a few drops of ethanol. Thereafter, the powder was calcined in air for 9 h at a temperature of  $1000^\circ\text{C}$ . Pristine  $\text{NiFe}_2\text{O}_4$  (NFO) were synthesized via a sol-gel auto-combustion method by mixing nickel nitrate, iron nitrate and glycine with a molar ratio of 1:2:1 in 10 mL total volume of distilled water. The solution was agitated at speed of 300 rpm and temperature of  $80^\circ\text{C}$  for 60 min until gelation occurs. Then, the as-prepared gel was heated on a sand bath for 6 h with a temperature-increasing step of  $50^\circ\text{C}$  up to  $350^\circ\text{C}$ , where the auto-ignition started suddenly, quickly, and violently with the flame. The typical experimental procedure used for the synthesis method is given as follows: first, the pristine synthesized STO powder is mixed with nickel nitrate, iron nitrate, and glycine with a molar ratio of 1:2:1, in 10 mL of distilled water. Thereafter, gelation was achieved after 30 min under magnetic agitation of the solution at a speed of 300 rpm and temperature of  $80^\circ\text{C}$ , followed by auto-ignition of the as-prepared gel in a sand bath for 6 h with a temperature increasing step of  $50^\circ\text{C}$  up to  $350^\circ\text{C}$ . In the end, the powder was kept for 9 h at a temperature of  $1100^\circ\text{C}$  to obtain a stabilized structure. Thus, the newly heterostructures, designated as of  $100-x\text{STO}/x\text{NFO}$ , were obtained at a different mass percentage of  $\text{NiFe}_2\text{O}_4$ . Otherwise, to get insight over system design, primordially we consider the structural, magnetic, and optical properties translated in terms of morphology.

### 2.2. Porous Heterostructure $100-x\text{STO}/x\text{NFO}$ Characterization

Phase identification and structural properties of starting nanomaterials calcined at  $1000^\circ\text{C}$  and composite ceramics, obtained at  $1100^\circ\text{C}$ , were determined by X-ray diffraction (Shimadzu LabX 6000; (Tokyo, Japan); diffractometer using  $\text{Cu-K}\alpha$  radiation ( $\lambda = 1.5406 \text{ \AA}$ ). The intensity and voltage of the X-ray source were set at 40 mA and 40 kV, respectively. The samples were scanned in reflection mode in the range  $20\text{--}80^\circ$  in  $2\theta$  with a step increment of  $0.02^\circ$  per step and a time per step of 0.2 s. Next, the morphology of the samples was studied using FE-SEM analysis, carried out on a Carl Zeiss NEON 40EsB; (Jena, Germany) with thermal Schottky field emission and accelerated Ga ions column. The FE-SEM micrographs were collected at different acceleration voltage and magnifications (1.8 kV, 50 kX 20 kV, 200 kX; 1.8 kV, 100 kX; and 5 kV, 150 kX). High-resolution electron micrographs of the calcined samples were taken by using a transmission electron microscope equipped with energy-dispersive X-ray spectroscopy (EDS) (Carl Zeiss LIBRA 200 MC

UHR-TEM); (Jena, Germany) (at magnification of 700 kX and accelerating voltage HV of 200 kV. The samples for high resolution transmission electron microscopy (HR-TEM) were prepared by ultrasonically dispersing the powder in isopropanol and allowing a drop of this to dry on a carbon-coated copper grid. The specific surface area and the pore size of the calcined samples were measured by gas adsorption–desorption isotherms method, using nitrogen as adsorbate at 78 K on a Quantachrome Nova 2200 analyzer and the samples being degassed for 4 h at 250 °C before testing. UV-Vis absorption spectrum of the  $_{75}\text{STO}/_{25}\text{NFO}$  nanocomposite in the wavelength range of 200–1100 nm was investigated by using a Shimadzu UV-Vis spectrophotometer. The energy of the bandgap ( $E_g$ ) was calculated using *Tauc's* method [35]. The variation of magnetic properties of the composite ceramics was studied by hysteresis loop obtained using a vibrating sample magnetometer (VSM, Princeton/Lakeshore M3900, Lake Shore Cryotronics, Westerville, OH, USA), at room temperature under a magnetic field in the range of  $\pm 10$  kOe. Dielectric properties of the calcined samples, in a wide temperature range (20–200 °C) and for the frequency  $2 \div 2 \times 10^6$  Hz, were carried out on the Ag-electrodes applied to the polished faces of the pelletized samples by using an Agilent E4980A Precision LCR Meter (Santa Clara, CA, USA). The cylindrical pellets with a diameter of 12 mm and 1.5 mm thickness were obtained at 140 MPa by using a Hand Press (Carver Inc., Model 4350.L, Wabash, IN, USA) and thermal treatment of 3 h at 700 °C.

### 3. Results

#### 3.1. Microstructural Characterization

The crystal structure and crystallinity of nanopowders, as pristine  $\text{SrTiO}_3$  and  $\text{NiFe}_2\text{O}_4$ , as well as  $_{75}\text{STO}/_{25}\text{NFO}$  porous-foam nanocomposite, were analyzed using X-ray diffraction analysis performed at room temperature in the 20–80° (2 $\theta$  degree) range (Figure 1).

The diffraction peaks can be indexed to ICSD no. 98-009-1899 for  $\text{SrTiO}_3$  and to ICSD no. 98-016-5448 for  $\text{NiFe}_2\text{O}_4$ , obtained via a sol-gel auto-combustion method without any other impurity or secondary phases. The pristine  $\text{SrTiO}_3$  obtained by solid-state reaction presents a cubic structure and a Sr-rich Ruddlesden-Popper (RP) phase [36,37]. After combining simultaneously, the above two synthetic methodologies,  $_{75}\text{STO}/_{25}\text{NFO}$  porous-foam nanocomposite was obtained as presented in Figure 1b. The diffraction peak of both, perovskite and inverse spinel, respectively are tracked together in the powder XRD pattern of the obtained foam. Thus, the sequential synthesis methodology addressed in this study allows the formation of a novel porous foam nanocomposite  $_{75}\text{STO}/_{25}\text{NFO}$ . Compared with the cubic perovskite and the inverse spinel-type structures, the diffraction lines of both  $\text{SrTiO}_3$  and  $\text{NiFe}_2\text{O}_4$  phases are present in the XRD pattern of the nanocomposites (Figure S1). The traditional crystallographic approach for structure determination (Rietveld refinement) was sufficient to confirm the crystal structure of the nanocomposites (Figures S2–S7). Rietveld analysis showed that the rutile  $\text{TiO}_2$  is present as a secondary phase because  $\text{SrTiO}_3$  is locally nonstoichiometric having Sr-rich RP phase. Using the normalized reference intensity ratio method (RIR), the percentage of rutile  $\text{TiO}_2$  phase in the  $_{75}\text{STO}/_{25}\text{NFO}$  porous-foam nanocomposite was determined to be about 2%.

According to data output from Rietveld refinement, as presented in Table 1, the crystallite size is 45 nm for  $\text{NiFe}_2\text{O}_4$  and 49 nm for  $\text{SrTiO}_3$ , respectively. In the case of composite, the Rietveld refinement was made by indexing the present phases, and their crystallite sizes were calculated by decomposing each corresponding diffraction peak, calculating FWHM. Therefore, the crystallite size values for NFO and STO were found to be 55 and 50 nm, respectively.

From the FE-SEM analysis of the  $_{75}\text{STO}/_{25}\text{NFO}$  porous-foam nanocomposite, the hierarchically porous material was formed by joint solid-state and sol-gel auto-combustion techniques. Hierarchical porosity is quite desirable for adsorption and photocatalytic processes and thus  $_{75}\text{STO}/_{25}\text{NFO}$  as visible-light-driven porous-foam nanocomposite with high contact surface area, high storage volume, ready mass transport, and a well-

controlled porosity, which grant to this material a very high adsorption capacity and a high photocatalytic efficiency.

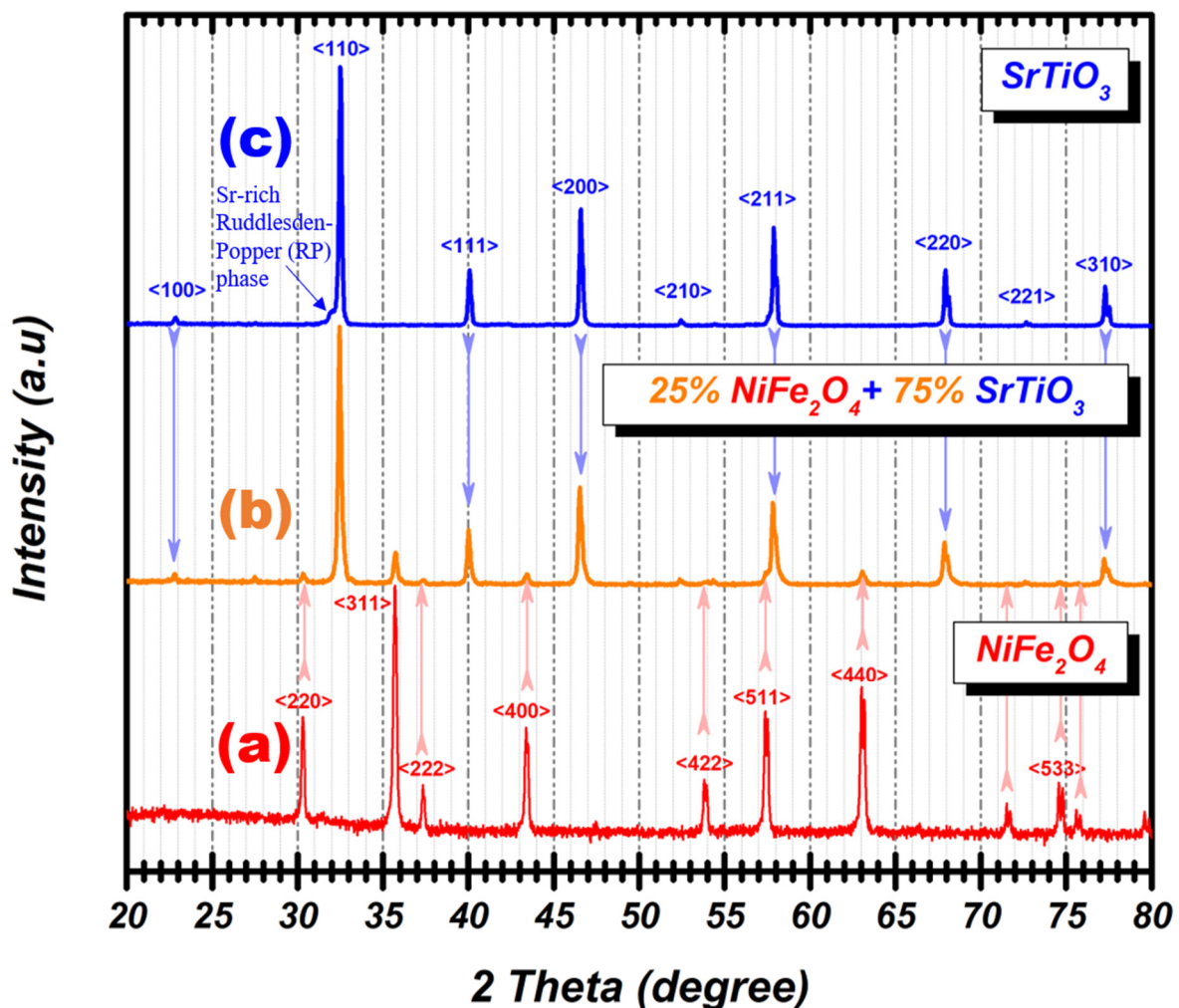


**Figure 1.** Powder XRD diffractograms of (a) pure cubic spinel phase  $\text{NiFe}_2\text{O}_4$  synthesized by sol-gel auto-combustion method, (b)  $_{75}\text{STO}/_{25}\text{NFO}$  porous-foam nanocomposite formed by joint solid-state and sol-gel auto-combustion techniques and annealed at  $1100\text{ }^\circ\text{C}$ , and (c) pristine cubic perovskite phase  $\text{SrTiO}_3$  synthesized by solid-state technique by mixing strontium carbonate and titanium dioxide with a molar ratio of 1:1 and thermal treated for 9 h at  $1000\text{ }^\circ\text{C}$ .

**Table 1.** Determined Cell Parameters after Rietveld refinement.

| Sample                    | Space Group  | Direct Cell Parameters ( $\text{\AA}$ ) | Direct Cell Volume ( $\text{\AA}^3$ ) | Reliability Factors |
|---------------------------|--------------|---|---------------------------------------|---------------------|
| $\text{SrTiO}_3$          | $Pm\bar{3}m$ | $a = b = c = 3.9034(3)$                 | $59.476(3)$                           | $0.796/0.899$       |
| $\text{NiFe}_2\text{O}_4$ | $Fd\bar{3}m$ | $a = b = c = 8.3402(3)$                 | $580.141(4)$                          | $1.79/3.97$         |
| $\text{TiO}_2$            | $P4_2/mnm$   | $a = b = 4.5912(2)$<br>$c = 2.9697(6)$  | $62.601(4)$                           | $5.01/13.2$         |

The pore formation mechanism in  $_{75}\text{STO}/_{25}\text{NFO}$  is shown in Figure 2. Particle interaction is dependent on sol-gel auto-combustion, which plays a key role in determining the morphology of the porous nanocomposite. Herein, a probable mechanism of pore formation in a highly porous framework is proposed and involves the self-assembly of  $\text{SrTiO}_3$  via the gelation process of the nickel nitrate, iron nitrate, and glycine. In the first step, polyhedral  $\text{SrTiO}_3$  nanoparticles were synthesized via the solid-state reaction of stron-

tium carbonate and titanium dioxide with a molar ratio of 1:1 and thermally treated in the air for 9 h at a temperature of 1000 °C. Next, these polyhedral SrTiO<sub>3</sub> nanoparticles are used as a template to form a 3D hierarchical xerogel composed of nickel and iron glycinate at a temperature of 80 °C for 60 min. Finally, the highly porous framework was converted to porous-foam <sub>75</sub>STO/<sub>25</sub>NFO nanocomposite on a sand bath for 6 h with a temperature-increasing step of 50 °C until auto-ignition occurs.

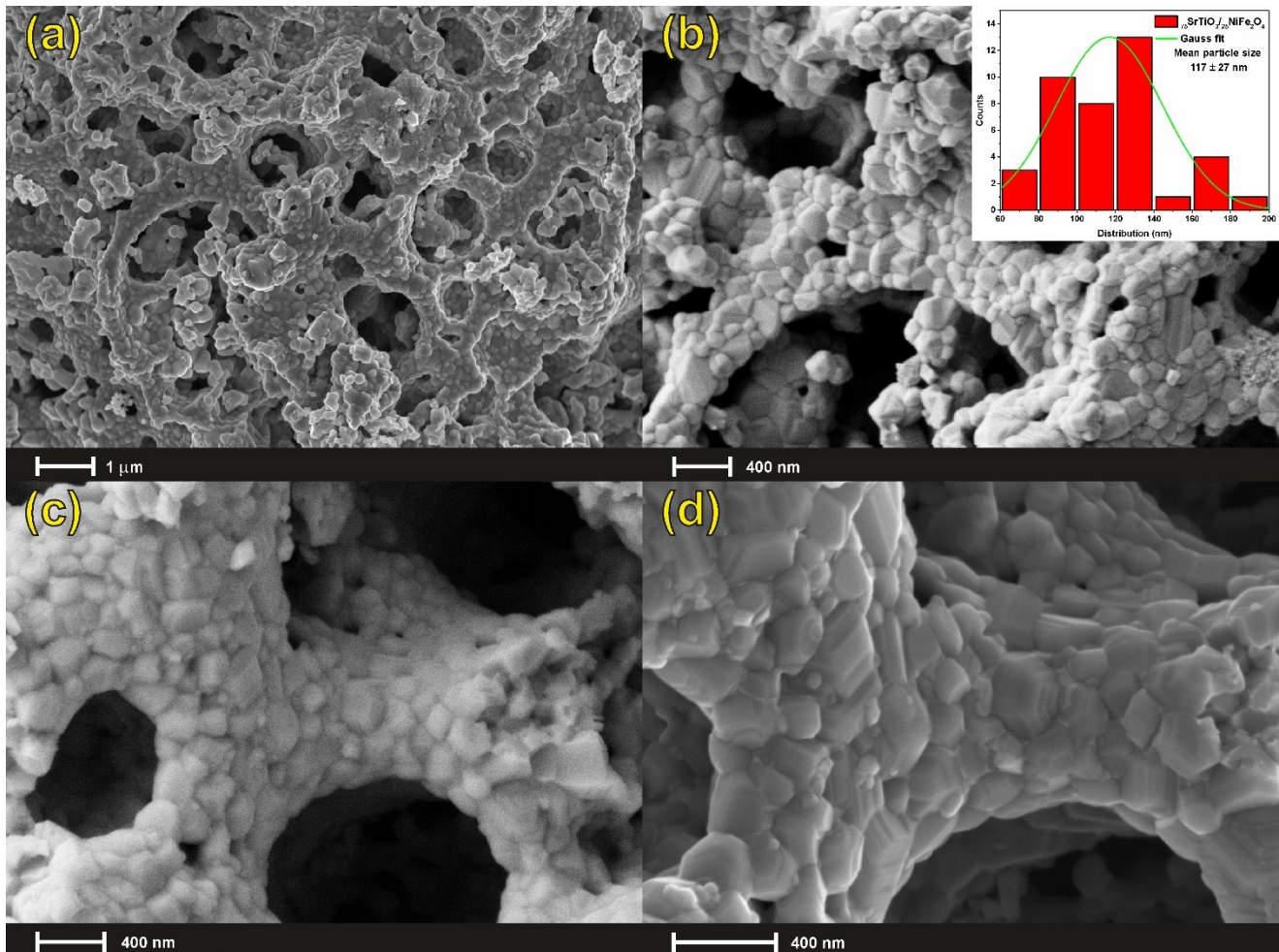


**Figure 2.** FE-SEM image of the porous structure (a) [scale 1 μm, electron high tension EHT = 5 KV and MAG = 10 kX], (b) [scale 400 nm, electron high tension EHT = 1.8 KV and MAG = 25 kX], (c) [scale 400 nm, electron high tension EHT = 5 kV and MAG = 30 kX], and (d) [scale 400 nm, electron high tension EHT = 5 KV and MAG = 45 kX], formed from the auto-combustion of hybrid 3D hierarchical xerogel composed of SrTiO<sub>3</sub> nanoparticles, nickel, and iron glycinate. Histogram (b-inserted) showing the particle size distribution of the <sub>75</sub>STO/<sub>25</sub>NFO [SD: ±27 nm].

To understand the morphological evolution of the <sub>75</sub>STO/<sub>25</sub>NFO nanocomposite into a hierarchical porous-foam structure, composition-dependent experiments were performed.

Figure 3 depicts the FE-SEM images of the SrTiO<sub>3</sub> template obtained from the solid-state reaction, pure NiFe<sub>2</sub>O<sub>4</sub> via a sol-gel auto-combustion, and its composition-dependent morphological evolution following different weights ratio  $x = 0, 50, 75,$  and 100 wt % of NiFe<sub>2</sub>O<sub>4</sub> in the <sub>100-x</sub>STO/<sub>x</sub>NFO system. Histograms, inserted in Figure 3, show the particle size distributions of the calcined starting materials and the <sub>50</sub>STO/<sub>50</sub>NFO and the <sub>25</sub>STO/<sub>75</sub>NFO. It is clear that with the NiFe<sub>2</sub>O<sub>4</sub> increasing content in system, the average particle size decreases, due to the smaller particle size of the ferrite.

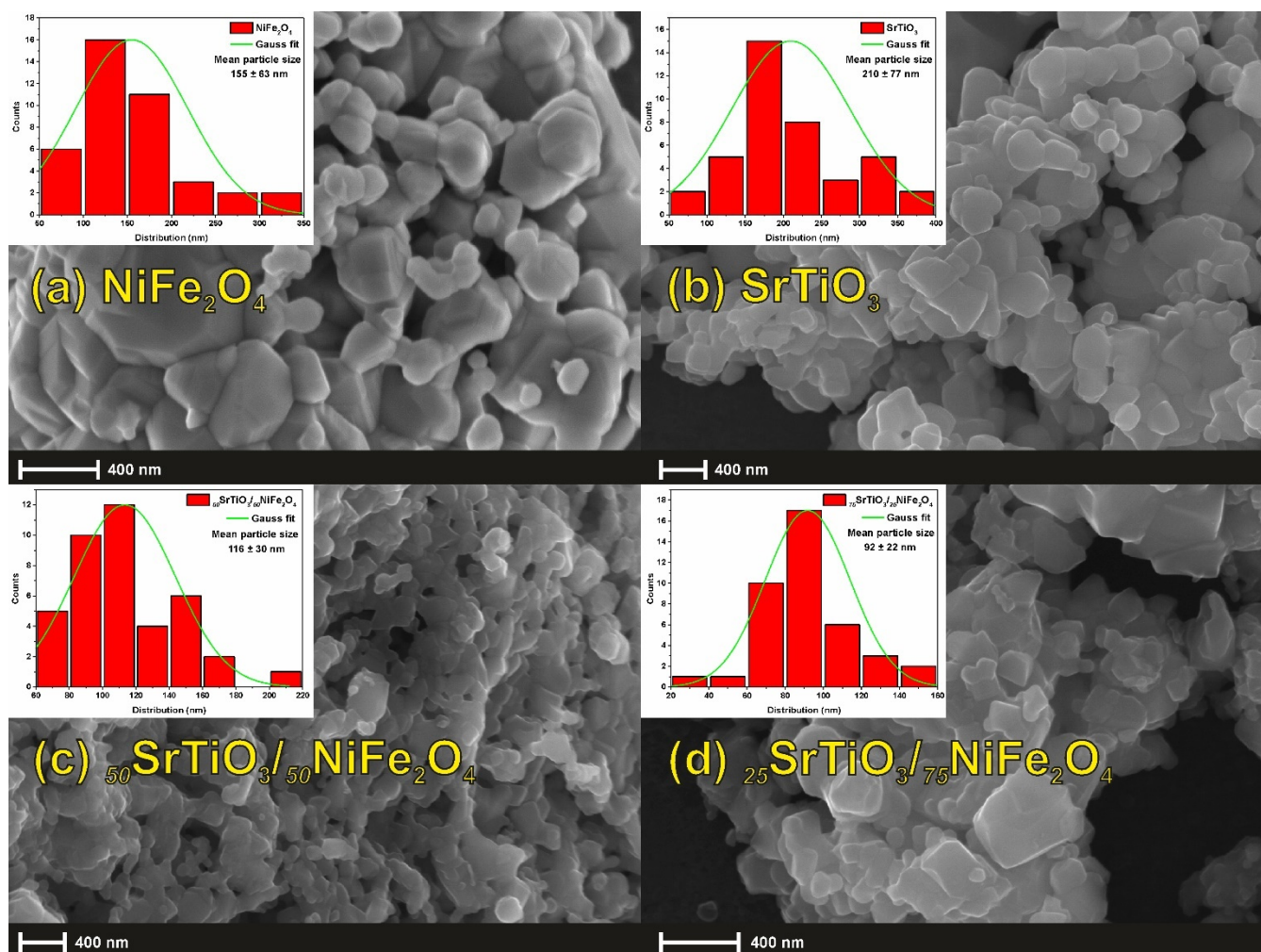


**Figure 3.** FE-SEM images of (a) pristine  $\text{NiFe}_2\text{O}_4$  [scale 400 nm, electron high tension EHT = 50 KV and MAG = 35 kX], (b) pristine  $\text{SrTiO}_3$  [scale 400 nm, electron high tension EHT = 20 KV and MAG = 20 kX], (c)  $_{50}\text{SrTiO}_3/_{50}\text{NiFe}_2\text{O}_4$  [scale 400 nm, electron high tension EHT = 20 KV and MAG = 25 kX], and (d)  $_{25}\text{SrTiO}_3/_{75}\text{NiFe}_2\text{O}_4$  [scale 400 nm, electron high tension EHT = 20 KV and MAG = 35 kX] composites. Histograms (inserted) showing the particle size distribution of the starting materials and the two composites by using the ImageJ software. The mean value of the particle size and the errors (standard deviation (SD)) were calculated by a Gaussian distribution applied to the histograms obtained.

As seen in Figure 3b, the template consists of highly nonuniform polyhedral nanoparticles. When these polyhedral nanoparticles were reacted with different amounts of aqueous  $\text{Ni}^{2+}$  and  $\text{Fe}^{3+}$  solutions (concerning composition stoichiometry) at room temperature in the presence of glycine, they form nonhomogeneous frameworks. The framework becomes more and more disordered as the amount of  $\text{NiFe}_2\text{O}_4$  increases, while highly porous-foam nanocomposite is obtained at the 3:1 mass ratio for  $\text{SrTiO}_3:\text{NiFe}_2\text{O}_4$  (Figure 2a–d), thereby indicating the optimal quantity of the reactants. Moreover, the selection of glycine, as fuel and chelating agent, in this synthesis was made according to its characteristic combustion temperature, because it affects the size of the crystallites, the structural stabilization, and the morphology. Glycine ignites at low temperatures, but the exothermic reaction is strong and violent with a large amount of gas released and high enthalpy leading to an increase in crystallites along with a good formation and high purity of the spinel-type structure. Our additional experiments reveal that when the concentration of the aqueous  $\text{Ni}^{2+}$  and  $\text{Fe}^{3+}$  glycinate was increased, the porous-foam-like structure partially collapsed to accommodate the formation of a nonhomogeneous system mixture of the two components.

To observe in more detail the morphology nature and lattice structure of  $_{75}\text{STO}/_{25}\text{NFO}$ , both transmission electron microscopy (TEM) and high-resolution TEM (HRTEM) imaging were performed. Figure 4a–d reveals the interconnected  $\text{NiFe}_2\text{O}_4$  nanoparticles with polyhedral  $\text{SrTiO}_3$  nanoparticles leading to porous nature of  $_{75}\text{STO}/_{25}\text{NFO}$  nanocomposite, as well as another interesting feature of small  $\text{NiFe}_2\text{O}_4$  particle attachments indicated by the yellow arrows present on the surface of the  $\text{SrTiO}_3$ . Furthermore, it can be observed from Figure 4d that the optimum 3:1 ratio of components forms bulk chains rather than a core-shell type structure. The TEM energy dispersive spectroscopy (TEM-EDS) elemental mapping images of  $_{75}\text{STO}/_{25}\text{NFO}$  nanocomposite reveals the uniform distribution of Sr, Ti, and O atoms in the nanocomposite (Figure S8) while Fe and Ni atoms appear attached and among to the surface and interconnected respectively to the perovskite phase.

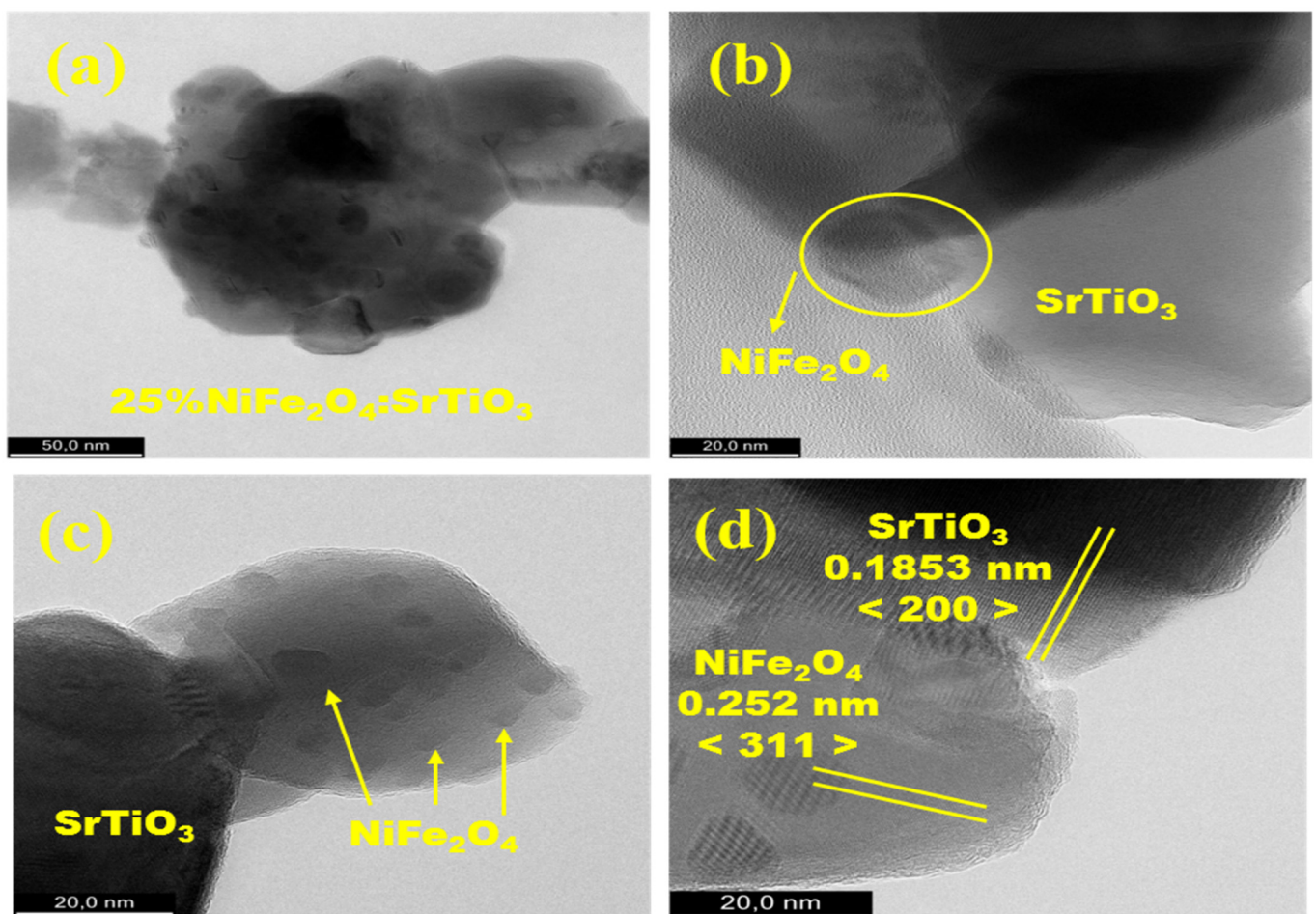


**Figure 4.** TEM image of the  $_{75}\text{STO}/_{25}\text{NFO}$  structure [scale 50nm] (a), HR-TEM image of the optimum hole interconnected  $\text{NiFe}_2\text{O}_4$  nanoparticles with polyhedral  $\text{SrTiO}_3$  nanoparticles [scale 20 nm] (b–d).

Figure 5 shows the nitrogen adsorption–desorption isotherms measurements of the composites and the corresponding average pore size distributions. It is found that all isotherms are of type IV with a  $\text{H}_3$  narrow hysteresis curve according to the IUPAC classification, characteristic of mesoporous materials (pores size in the range of 2.0–50.0 nm) [38]. The type of hysteresis loop provides information about the shape and connectivity of the inner pores [39], which plays an important role in the rate of gas adsorption. In our materials,  $\text{H}_3$  type hysteresis loops are associated with a porous structure that has pores with irregular size and shapes [40]. For all analyzed samples a gradual increase of the amount of  $\text{N}_2$  adsorbed from relatively small values of relative pressure is observed. However, the sudden increase in the amount of  $\text{N}_2$  adsorbed at low values of relative pressure,  $P/P_0$ , proves that the samples present relatively large specific surface areas. Moreover, hys-

teresis loop at high relative pressures can be found, indicating the presence of porous structure, especially for the  $_{75}\text{STO}/_{25}\text{NFO}$  nanocomposite. The pore size distribution curve of  $_{75}\text{STO}/_{25}\text{NFO}$  shows a monomodal distribution with average pore diameters of between 13.97 and 15.86 nm (calculated from BJH desorption and adsorption isotherms, respectively) [41]. The  $_{50}\text{STO}/_{50}\text{NFO}$  exhibits a linear pore distribution with average pore diameter between 8.23 nm and 7.44 nm and the  $_{25}\text{STO}/_{75}\text{NFO}$  composite shows a narrow pore-size distribution with pore size of about 7.5 nm. Moreover, t-Plot micropore volume [42] is negative for all composites, meaning the samples do not contain micropores. The calculated textural characteristics of the samples, by using BET, BJH and t-plots methods, are summarized in Table 2. As expected,  $_{75}\text{STO}/_{25}\text{NFO}$  nanocomposite has the highest  $S_{\text{BET}}$  and Langmuir surface area, of 52 and  $75 \text{ m}^2 \text{ g}^{-1}$ , respectively, as well as pore volume, suggesting that meso-pores make the largest contribution to the surface area. In this way, meso-porosity is produced in  $_{75}\text{STO}/_{25}\text{NFO}$  composite leading to an ordered porous structure, as confirmed by FE-SEM and HR-TEM.  $_{50}\text{STO}/_{50}\text{NFO}$  and  $_{25}\text{STO}/_{75}\text{NFO}$  composites showed smaller  $S_{\text{BET}}$  and pore volume, suggesting the entry of the nitrogen gas molecules was partially restricted [43]. Nearly double values of pore volume and diameter (0.148 nm and 15.86 nm, respectively) and larger size of specific surface area suggest that  $_{75}\text{STO}/_{25}\text{NFO}$  nanocomposite can provide more active sites and adsorb more reactive species in further photocatalytic experiments.

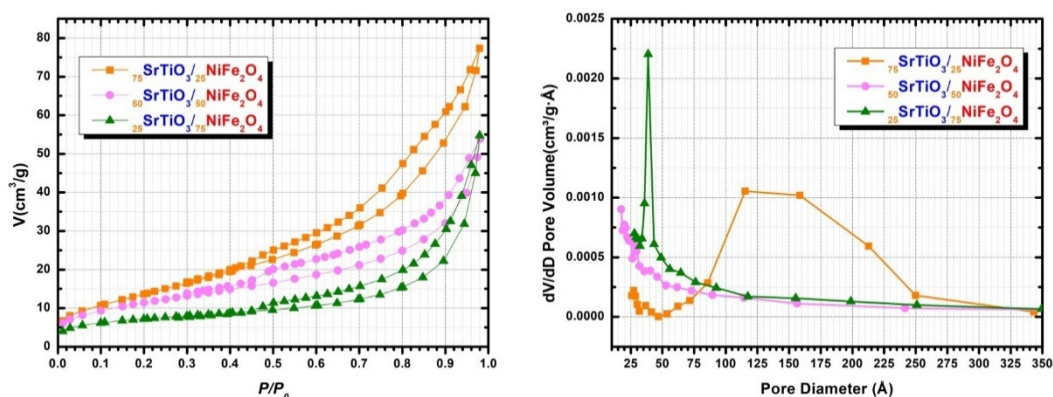


**Figure 5.** Nitrogen adsorption isotherms of the nanocomposites (left), and the corresponding average pore size distributions (right).

**Table 2.** Textural characteristic of the obtained nanocomposites.

| Sample                            | BET Surface Area ( $\text{m}^2 \text{ g}^{-1}$ ) | Langmuir Surface Area ( $\text{m}^2 \text{ g}^{-1}$ ) | Volume of Pores (Adsorption) ( $\text{cm}^3 \text{ g}^{-1}$ ) | Volume of Pores (Desorption) ( $\text{cm}^3 \text{ g}^{-1}$ ) | Average Pore Width (Adsorption) (nm) | Average Pore Width (Desorption) (nm) |
|-----------------------------------|--|---|---|---|--------------------------------------|--------------------------------------|
| $_{75}\text{STO}/_{25}\text{NFO}$ | $52 \pm 1$                                       | $75 \pm 1$  | $0.148 \pm 0.004$   | $0.146 \pm 0.004$   | $15.86 \pm 0.91$                     | $13.97 \pm 0.78$                     |
| $_{50}\text{STO}/_{50}\text{NFO}$ | $39 \pm 1$                                       | $59 \pm 3$  | $0.082 \pm 0.001$   | $0.074 \pm 0.003$   | $8.30 \pm 0.77$                      | $7.44 \pm 0.97$                      |
| $_{25}\text{STO}/_{75}\text{NFO}$ | $25 \pm 2$                                       | $36 \pm 1$  | $0.078 \pm 0.002$   | $0.074 \pm 0.006$   | $7.76 \pm 1.12$                      | $7.36 \pm 0.64$                      |

Figure 6 shows the UV-Vis absorbance spectra of the  $_{75}\text{STO}/_{25}\text{NFO}$  nanocomposite as a hierarchical porous-foam structure to reveal the optical properties. It is very well studied in the literature that the absorption band of pure  $\text{SrTiO}_3$  sharply drops at about 388 nm whereas that of the pure  $\text{NiFe}_2\text{O}_4$  continuously extends to the visible-light region ( $300 \text{ nm} < \lambda < 1000 \text{ nm}$ ). This means that  $\text{SrTiO}_3$  only has a response to the UV light but the pure  $\text{NiFe}_2\text{O}_4$  can respond to both the UV and visible light. Using Tauc's relation:  $((\alpha h\nu)^2 = A(h\nu - E_g))$ , the bandgap of 1.5 eV is determined by extrapolating the linear portion of the curve to the energy axis as shown in Figure 6 (inset). We can note that the  $_{75}\text{STO}/_{25}\text{NFO}$  nanocomposite with a hierarchical porous-foam structure has extended absorption spectra into the visible light region. Interestingly, it is noteworthy that the

characteristic absorption peak of NiFe<sub>2</sub>O<sub>4</sub> at about 750 nm still excites in that of synthesized hierarchical porous-foam and is certified further to the earlier reports about the similar composite nanoparticles and from this point of view, the heterojunctions of SrTiO<sub>3</sub>/NiFe<sub>2</sub>O<sub>4</sub> bring up the complementarity that should exist between the two components (Table 3). Note that the study of these nanomaterials is a complex one, and here is presented only the first stage, in which we wanted to highlight an extremely interesting phenomenon of colloidal attachment of two reference nanomaterials in current technological and environmental applications.

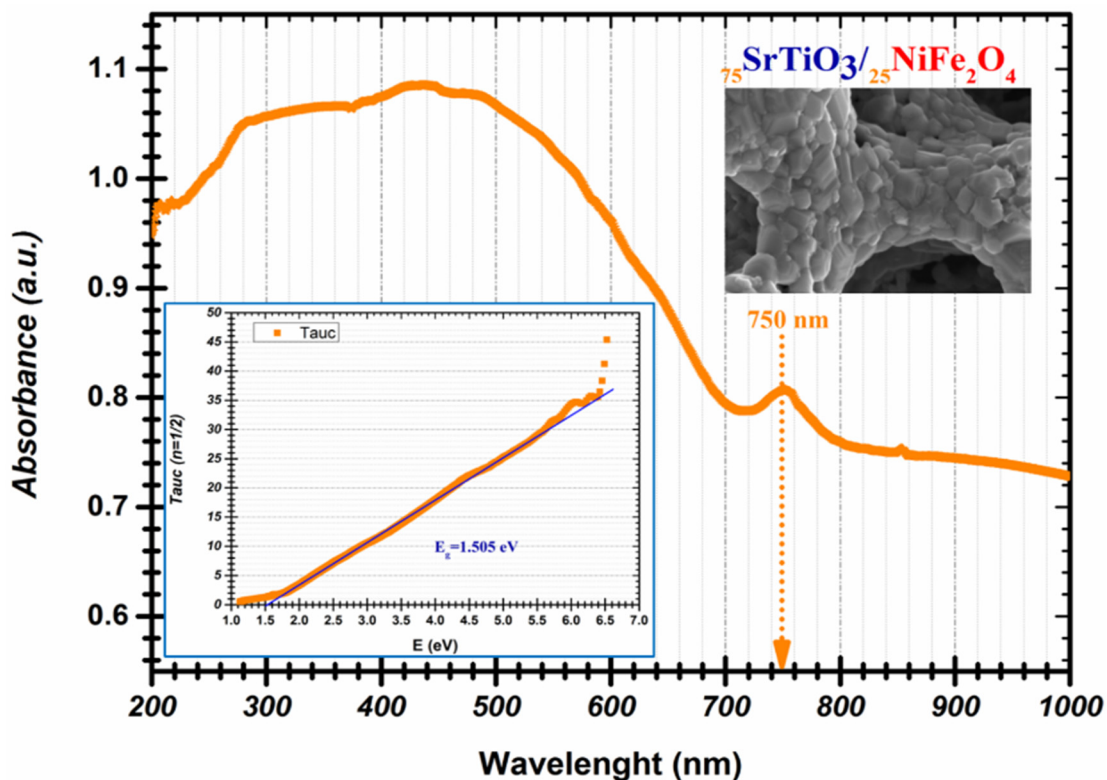


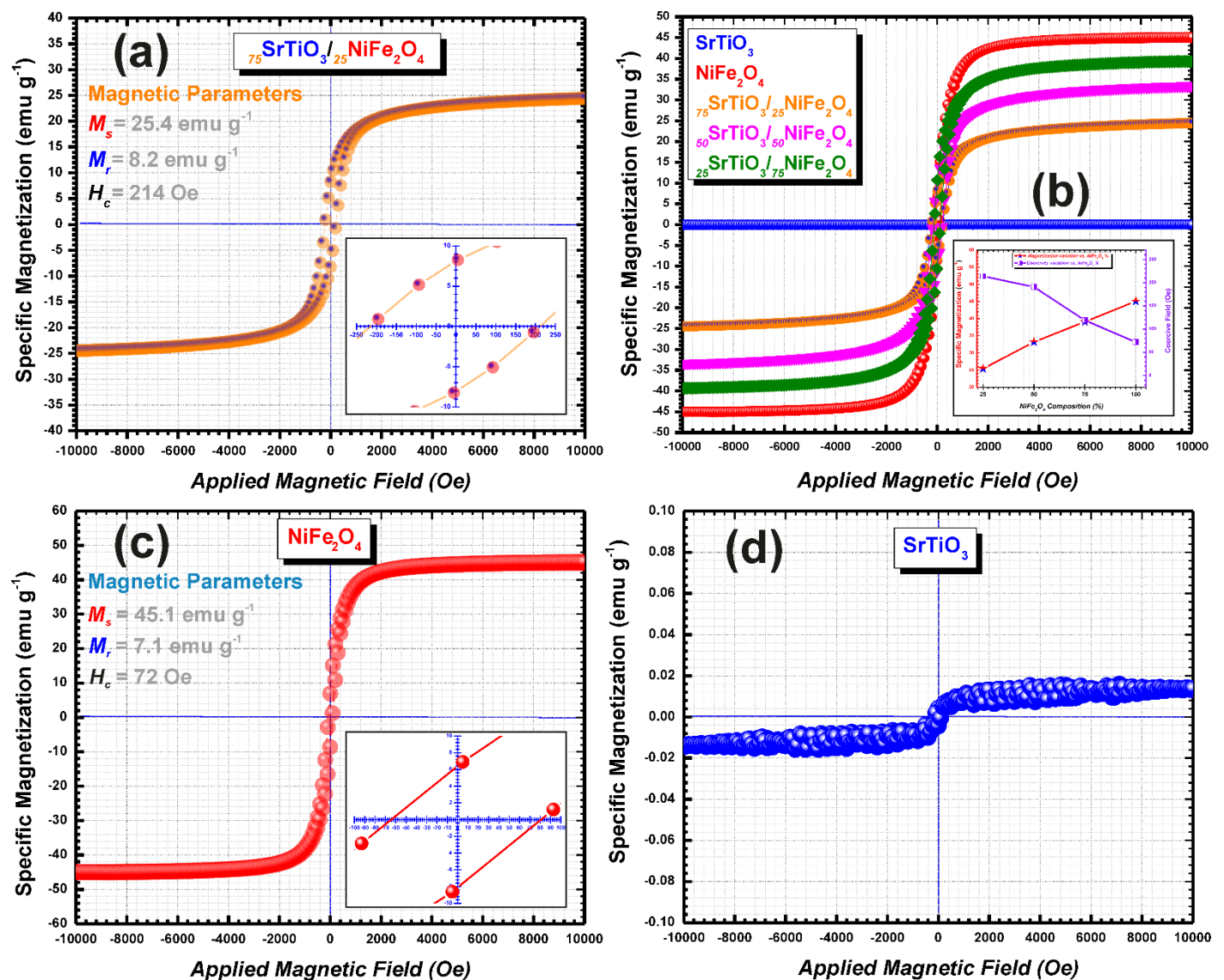
Figure 6. UV-vis DRS of 75STO/25NFO nanocomposite as hierarchical porous-foam structure and (Inset) corresponding Tauc plot for bandgap determination.

Table 3. Bandgap values of NiFe<sub>2</sub>O<sub>4</sub>, SrTiO<sub>3</sub> and SrTiO<sub>3</sub>/NiFe<sub>2</sub>O<sub>4</sub> composite thereof.

| Compound   | Composition  | Band Gap Values (eV) | References |
|--|--|----------------------|------------|
| SrTiO <sub>3</sub>   | pristine   | 3.20                 | [7]        |
| SrTiO <sub>3</sub>   | pristine   | 3.15                 | [34]       |
| NiFe <sub>2</sub> O <sub>4</sub>                                   | pristine   | 1.70                 | [44]       |
| NiFe <sub>2</sub> O <sub>4</sub>                                   | pristine   | 1.82                 | [34]       |
| NiFe <sub>2</sub> O <sub>4</sub>                                   | pristine   | 1.40                 | [45]       |
| γ-Fe <sub>2</sub> O <sub>3</sub> @NiFe <sub>2</sub> O <sub>4</sub> | 50% γ-Fe <sub>2</sub> O <sub>3</sub><br>50% NiFe <sub>2</sub> O <sub>4</sub> | 1.38                 | [45]       |
| SrTiO <sub>3</sub> /NiFe <sub>2</sub> O <sub>4</sub>               | 15% SrTiO <sub>3</sub><br>85% NiFe <sub>2</sub> O <sub>4</sub>               | 1.42                 | [34]       |
| 75STO/25NFO  | 75% SrTiO <sub>3</sub><br>25% NiFe <sub>2</sub> O <sub>4</sub>               | 1.50                 | This Study |

Room temperature hysteresis loops of our pure and composite materials are represented in Figure 7. Indeed, as shown in Figure 7d the recorded room temperature hysteresis loops reveal that the pure SrTiO<sub>3</sub> has no magnetism; however, pristine NiFe<sub>2</sub>O<sub>4</sub> nanopar-

ticles show a ferromagnetic behavior with the saturation magnetization ( $M_s$ ) of about  $45 \text{ emu g}^{-1}$  (Figure 7c).



**Figure 7.** Room temperature hysteresis loops of the (a)  $75\text{STO}/25\text{NFO}$  nanostructure, (b) all composites synthesized with different spinel phase percentage together with inset graph showing the magnetization and coercivity variation with spinel phase ratios, (c) pristine  $\text{NiFe}_2\text{O}_4$  nanoparticles with inset graph showing the loop at near-zero magnetic field, and (d) pristine  $\text{SrTiO}_3$  nanoparticles.

Considering the presence of the non-magnetic  $\text{SrTiO}_3$ , the  $M_s$  values for the synthesized composites with different ratios of  $\text{NiFe}_2\text{O}_4$  from 25% up to 75% (Figure 7b), are lower than that of the pure spinel phase and they are between 25 and  $39 \text{ emu g}^{-1}$  (see Table 4). It is interesting to note that the magnetization does not decrease proportionally to the amount of non-magnetic  $\text{SrTiO}_3$  present in the composition of samples (Figure 7b). Moreover, the highest coercivity value is determined for the  $75\text{STO}/25\text{NFO}$  sample, maybe due to the high magneto crystalline anisotropy, emphasizing the same trend described vide-supra. The mentioned phenomenon needs more experimental work corroborated with theoretical simulation to unequivocally assess the magnetic properties of the as-prepared nanocomposites in hierarchical assembly as well in nonhomogeneous form.

**Table 4.** Magnetic properties of NiFe<sub>2</sub>O<sub>4</sub>, SrTiO<sub>3</sub>, and SrTiO<sub>3</sub>/NiFe<sub>2</sub>O<sub>4</sub> composites thereof.

| Sample   | Specific Magnetization (emu g <sup>-1</sup> ) | Remanent Magnetization (emu g <sup>-1</sup> ) | Coercive Field (Oe) | References |
|--|---|---|---------------------|------------|
| SrTiO <sub>3</sub>   | -   | -   | -                   | This Study |
| 75SrTiO <sub>3</sub> /25NiFe <sub>2</sub> O <sub>4</sub>                       | 25.4  | 8.2   | 214                 | This Study |
| 50SrTiO <sub>3</sub> /50NiFe <sub>2</sub> O <sub>4</sub>                       | 33.2  | 10.5  | 191                 | This Study |
| 25SrTiO <sub>3</sub> /75NiFe <sub>2</sub> O <sub>4</sub>                       | 39.1  | 10.2  | 119                 | This Study |
| NiFe <sub>2</sub> O <sub>4</sub>   | 45.1  | 7.1   | 72                  | This Study |
| SrTiO <sub>3</sub> /NiFe <sub>2</sub> O <sub>4</sub> porous nanotubes          | 10  | n.a   | n.a                 | [8]        |
| SrTiO <sub>3</sub> /NiFe <sub>2</sub> O <sub>4</sub> nanoparticle-in nanotubes | 18  | n.a   | n.a                 | [8]        |
| NiFe <sub>2</sub> O <sub>4</sub>   | 40  | n.a   | n.a                 | [34]       |
| 85% NiFe <sub>2</sub> O <sub>4</sub><br>15% SrTiO <sub>3</sub>                 | 23.3  | n.a   | n.a                 | [34]       |

### 3.2. Comparative Analysis of the Dielectric Properties

The evolution with the frequency of the real and imaginary parts of permittivity for the starting material and the composites prepared is comparatively presented in Figure 8a–h. For a better understanding of the extrinsic permittivity of the composite materials, SrTiO<sub>3</sub> was prepared under the same conditions as the composites for the dielectric analysis. The frequency dependence of real and imaginary part of permittivity of pure pristine SrTiO<sub>3</sub> ceramic at few temperatures are shown in Figure 8a,e, showing a different behavior compared to that of composites. At low frequency, the sample presents a strong decay and at high frequency (10<sup>5</sup>–10<sup>6</sup>) Hz, where all the extrinsic phenomena were canceled, the permittivity tends to its intrinsic values ~1100.

On the other hand, the real part of permittivity vs. frequency indicates rather similar dielectric behaviors for all composites. The frequency dispersion is higher with increasing temperature and this increase is enhanced at lower frequencies. The 75STO/25NFO composite shows higher permittivity at low frequencies, increasing with temperature. For example, at  $f = 1$  kHz, the permittivity assumes values of about 457 at 25 °C and 1072 at 120 °C for the 75STO/25NFO, while for the 25STO/75NFO composite, of about 131 and 710 at the same temperatures, respectively. Imaginary parts of permittivity (Figure 8f–h) show a strong decrease with frequency from  $2 \times 10^4$  to ~2 for 75STO/25NFO and  $3 \times 10^4$  to 10 for 25STO/75NFO composites, respectively, at the frequency between 20 Hz to 10<sup>6</sup> Hz and 120 °C. Both composites show a low-frequency decay of the real and imaginary part of permittivity, which strongly increases with temperature. However, apart from the linear variation observed in the case of 50STO/50NFO composite, the two materials appear to be temperature independent with increasing frequency and temperature. While for 50STO/50NFO composite, these extrinsic mechanisms seem to be canceled for frequency higher than 10<sup>5</sup> Hz, in case of the 75STO/25NFO and 25STO/75NFO composites, they continue to exist in all investigated frequency range. The observed differences show that extrinsic contributions are slightly different in these types of composites. The extrinsic contributions are due to Maxwell–Wagner relaxations and dc-conductivity caused by the slow-charged species activated at low frequencies and high temperatures [46]. The Maxwell–Wagner relaxation is related to inhomogeneities and interfaces [47], and it seems that the better dielectric characteristics obtained for slightly temperature-dependent 75STO/25NFO composite are a consequence of different microstructural properties, e.g., hierarchical porous-foam morphology by particle attachment. At high frequency (around 10<sup>5</sup> Hz), where the charge defect-associated relaxations are no longer active, the permittivity tends to its intrinsic value [48,49]. For this frequency, at 120 °C, values around ~320 for 75STO/25NFO (independent with temperature), ~250 for 75STO/25NFO (temperature-dependent) and ~190 for 25STO/75NFO (temperature dependent), are found. The dielectric losses at high frequencies (1 MHz) (Figure 8l–n) seem to be independent of the composite type, temperature-dependent and are in the range of 0.02–0.18 for temperatures between 20 and 200 °C.

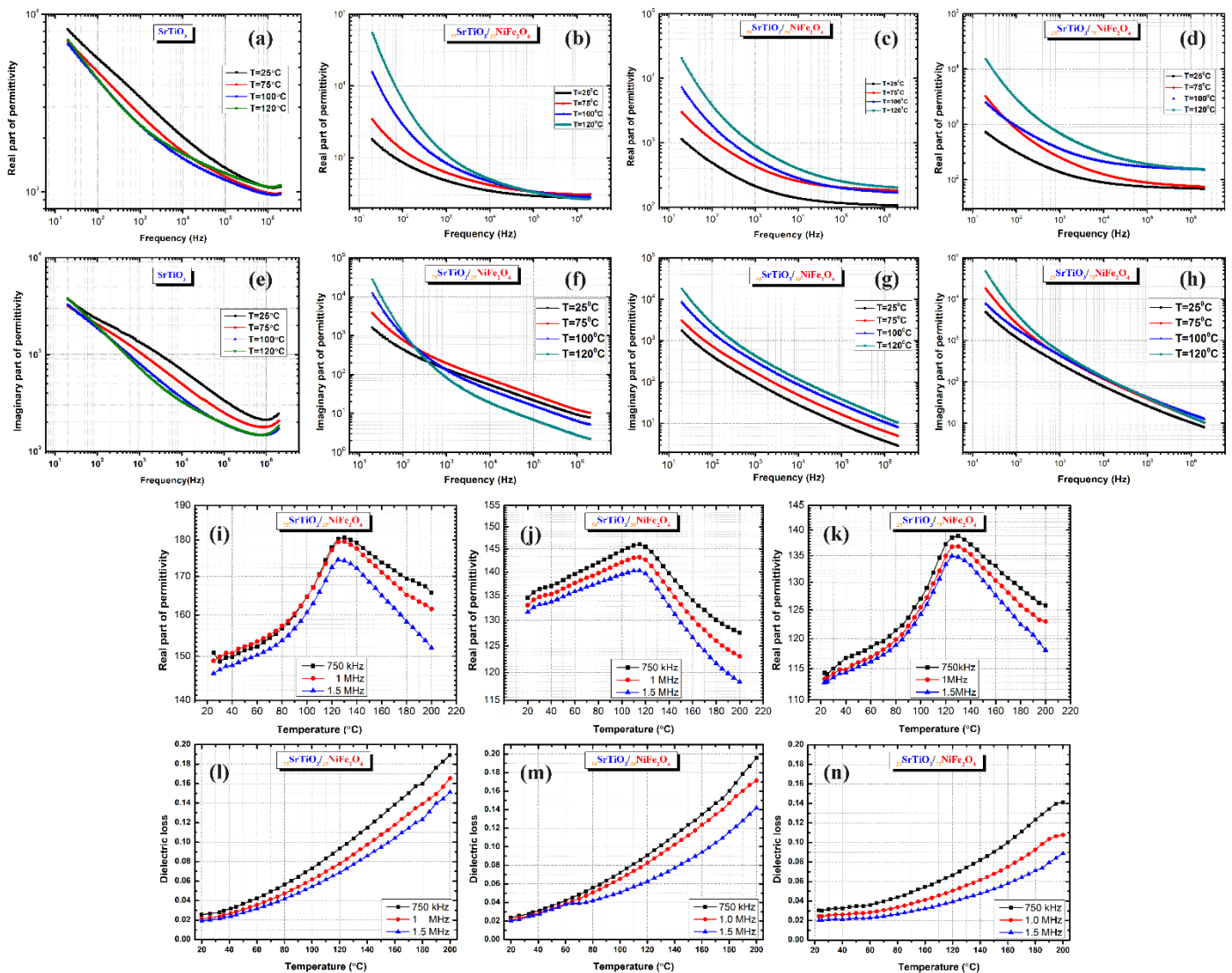


**Figure 8.** Dielectric dispersion at few temperatures of the materials: (a,e) real and imaginary parts of permittivity of the SrTiO<sub>3</sub>; and (b–d) real part of permittivity and (f–h) imaginary part of permittivity of 100–*x*STO/*x*NFO composites. Temperature dependence of the dielectric characteristics at a few selected frequencies for 100–*x*STO/*x*NFO composites: (i–k) permittivity; (l–n) tangent loss.

The temperature dependence of permittivity shows some differences for the composites according to the composition (Figure 8i–k). A broad permittivity maximum can be detected in the range of about 120–140 °C for all composites and it originates from a relaxor character or a reduction of ferroelectric character [50,51]. The shape and the position of the permittivity maximum are affected by an extrinsic dielectric effect that tends to cover the intrinsic ferroelectric behavior in the composites and the permittivity decreases with temperature and frequency. The shape of the permittivity maximum might be explained by local compositional variations and morphological differences [52].

#### 4. Conclusions

Sequential synthesis methodology addressed in this study enables the successful fabrication of 75STO/25NFO as porous-foam in nature by joint solid-state and sol-gel auto-combustion technique. The diffraction peak of both, perovskite and inverse spinel, respectively, were tracked together in the powder XRD pattern of the obtained composite. The 75STO/25NFO composite exhibits a powerful visible light response with a band gap energy of 1.505 eV and a value of the room temperature permittivity of 457. In addition,

$_{75}\text{STO}/_{25}\text{NFO}$  composite shows higher permittivity at low frequencies, which is proportional to the temperature increase. Morphological analyses performed by FE-SEM and HRTEM reveal that the consolidation of particles occurs by exact stacking of  $\text{NiFe}_2\text{O}_4$  particles along crystal facets of  $\text{SrTiO}_3$ .  $_{75}\text{STO}/_{25}\text{NFO}$  nanocomposite showed the highest  $S_{\text{BET}}$  and Langmuir surface area values, of 52 and  $75 \text{ m}^2 \text{ g}^{-1}$ , respectively, as well as pore volume, which can suggest that meso-pores make the largest contribution to the surface area. The values of the specific magnetization increased from 25.4 to  $45.1 \text{ emu g}^{-1}$  when the ratio  $x$  in  $_{100-x}\text{STO}/_x\text{NFO}$  increases from 25 to 100. The coercivity showed the highest value of 214 Oe for the  $_{75}\text{STO}/_{25}\text{NFO}$  sample. The nanocomposite can be considered as the famous heterojunction connection by sequential synthesis methodology addressed in this study with emphasis on the colloidal assembly of the attachment of the  $\text{NiFe}_2\text{O}_4$  particles in the presence of  $\text{SrTiO}_3$ .

**Supplementary Materials:** The following supporting information can be downloaded at: <https://www.mdpi.com/article/10.3390/nano12010138/s1>, Figure S1. The superimposed XRD patterns of perovskite phases ( $\text{SrTiO}_3$ ) synthesized with different ratios of spinel phase ( $\text{NiFe}_2\text{O}_4$ ); Figure S2. The Rietveld refinement of the  $_{75}\text{STO}/_{25}\text{NFO}$ . Black solid line is the best fits to the experimental data, the blue line represents the differences between the experimental and calculated data while the vertical markers represent the Bragg peaks positions in blue for Cubic perovskite phase, in red for Cubic spinel phase and in green for Tetragonal  $\text{TiO}_2$  phase; Figure S3. Le Bail refinement from laboratory XRD patterns at RT The Rietveld refinement of  $\text{SrTiO}_3$  nanoparticles. Black solid line is the best fits to the experimental data, the blue line represents the differences between the experimental and calculated data while the vertical markers represent the Bragg peaks positions in blue for Cubic perovskite phase and in red for Ruddlesden–Popper phase; Figure S4. The Rietveld refinement of  $\text{SrTiO}_3$  with 25% of  $\text{NiFe}_2\text{O}_4$ . Black solid line is the best fits to the experimental data, the blue line represents the differences between the experimental and calculated data while the vertical markers represent the Bragg peaks positions in blue for Cubic perovskite phase and in red for Cubic spinel phase and in green for Tetragonal  $\text{TiO}_2$  phase; Figure S5. The Rietveld refinement of  $\text{SrTiO}_3$  with 50% of  $\text{NiFe}_2\text{O}_4$ . Black solid line is the best fits to the experimental data, the blue line represents the differences between the experimental and calculated data while the vertical markers represent the Bragg peaks positions in blue for Cubic perovskite phase, in green for Tetragonal perovskite phase and in red Cubic spinel phase; Figure S6. The Rietveld refinement of  $\text{SrTiO}_3$  with 75% of  $\text{NiFe}_2\text{O}_4$ . Black solid line is the best fits to the experimental data, the blue line represents the differences between the experimental and calculated data while the vertical markers represent the Bragg peaks positions in blue for Cubic perovskite phase, in green for Tetragonal perovskite phase and in red Cubic spinel phase; Figure S7. The Rietveld refinement of  $\text{NiFe}_2\text{O}_4$  nanoparticles. Black solid line is the best fits to the experimental data, the blue line represents the differences between the experimental and calculated data while the vertical markers represent the Bragg peaks positions in blue for Cubic spinel phase; Figure S8. TEM dark field image of  $\text{NiFe}_2\text{O}_4$  particle attachment on  $\text{SrTiO}_3$  polyhedral nanoparticles (a) and the corresponding elemental mapping for all elements Fe, Ni, Sr, Ti, O (b) Sr, Ti (c) and Fe, Ni (d).

**Author Contributions:** Conceptualization, D.G., A.-R.I., M.N.P., N.L., L.L. and A.I.B.; Data curation, G.A., N.L. and A.A.; Formal analysis, I.B.-A., R.B., M.A.B. and T.R.; Investigation, I.B.-A., D.G., C.M., R.B., G.A., N.L., M.A.B., T.R. and G.B.; Methodology, D.G., M.N.P. and A.I.B.; Project administration, A.-R.I. and A.I.B.; Resources, A.I.B., A.-R.I. and M.N.P.; Supervision, A.-R.I. and L.L.; Validation, I.B.-A., T.R., G.B. and L.L.; Writing—original draft, I.B.-A., A.I.B., D.G., C.M. and T.R.; Writing—review & editing, N.L., A.A., D.G., A.-R.I. and A.I.B. All authors have read and agreed to the published version of the manuscript.

**Funding:** This work was supported by a grant of the Ministry of Research, Innovation and Digitization, CNCS/CCCDI-UEFISCDI, project number PN-III-P1-1.1-TE-2019-2037, within PNCDI III and by a grant of the Ministry of Research, Innovation and Digitization, CNCS/CCCDI-UEFISCDI, project number PN-III-P2-2.1-PED-2019-4215, within PNCDI III.

**Data Availability Statement:** The data presented in this study are available from the corresponding author on request.

**Conflicts of Interest:** The authors declare no conflict of interest.

## References

1. Zheng, H.; Zhan, Q.; Zavaliche, F.; Sherburne, M.; Straub, F.; Cruz, M.P.; Chen, L.-Q.; Dahmen, U.; Ramesh, R. Controlling self-assembled perovskite–spinel nanostructures. *Nano Lett.* **2006**, *6*, 1401–1407. [[CrossRef](#)] [[PubMed](#)]
2. Lendlein, A.; Trask, R.S. Multifunctional materials: Concepts, function-structure relationships, knowledge-based design, translational materials research. *Multifunct. Mater.* **2018**, *1*, 10201. [[CrossRef](#)]
3. Gibson, R.F. A review of recent research on mechanics of multifunctional composite materials and structures. *Compos. Struct.* **2010**, *92*, 2793–2810. [[CrossRef](#)]
4. Ren, K.; Zheng, R.; Xu, P.; Cheng, D.; Huo, W.; Yu, J.; Zhang, Z.; Sun, Q. Electronic and Optical Properties of Atomic-Scale Heterostructure Based on MXene and MN (M= Al, Ga): A DFT Investigation. *Nanomaterials* **2021**, *11*, 2236. [[CrossRef](#)] [[PubMed](#)]
5. Ren, K.; Sun, M.; Luo, Y.; Wang, S.; Yu, J.; Tang, W. First-principle study of electronic and optical properties of two-dimensional materials-based heterostructures based on transition metal dichalcogenides and boron phosphide. *Appl. Surf. Sci.* **2019**, *476*, 70–75. [[CrossRef](#)]
6. Chen, Y.; Lai, Z.; Zhang, X.; Fan, Z.; He, Q.; Tan, C.; Zhang, H. Phase engineering of nanomaterials. *Nat. Rev. Chem.* **2020**, *4*, 243–256. [[CrossRef](#)]
7. Reunchan, P.; Ouyang, S.; Umezawa, N.; Xu, H.; Zhang, Y.; Ye, J. Theoretical design of highly active SrTiO<sub>3</sub>-based photocatalysts by a codoping scheme towards solar energy utilization for hydrogen production. *J. Mater. Chem. A* **2013**, *1*, 4221–4227. [[CrossRef](#)]
8. Jing, P.; Du, J.; Wang, J.; Lan, W.; Pan, L.; Li, J.; Wei, J.; Cao, D.; Zhang, X.; Zhao, C.; et al. Hierarchical SrTiO<sub>3</sub>/NiFe<sub>2</sub>O<sub>4</sub> composite nanostructures with excellent light response and magnetic performance synthesized toward enhanced photocatalytic activity. *Nanoscale* **2015**, *7*, 14738–14746. [[CrossRef](#)]
9. Vivek, S.; Geetha, P.; Saravanan, V.; Kumar, A.S.; Lekha, C.S.C.; Sudheendran, K.; Anantharaman, M.R.; Nair, S.S. Magnetolectric coupling in strained strontium titanate and Metglas based magnetolectric trilayer. *J. Alloys Compd.* **2019**, *789*, 1056–1061. [[CrossRef](#)]
10. Coey, J.M.D.; Venkatesan, M.; Stamenov, P. Surface magnetism of strontium titanate. *J. Phys. Condens. Matter* **2016**, *28*, 485001. [[CrossRef](#)] [[PubMed](#)]
11. Kleemann, W.; Dec, J.; Tkach, A.; Vilarinho, P.M. SrTiO<sub>3</sub>—Glimpses of an Inexhaustible Source of Novel Solid State Phenomena. *Condens. Matter* **2020**, *5*, 58. [[CrossRef](#)]
12. Bannikov, V.V.; Shein, I.R.; Kozhevnikov, V.L.; Ivanovskii, A.L. Magnetism without magnetic ions in non-magnetic perovskites SrTiO<sub>3</sub>, SrZrO<sub>3</sub> and SrSnO<sub>3</sub>. *J. Magn. Magn. Mater.* **2008**, *320*, 936–942. [[CrossRef](#)]
13. Ke, H.; Zhang, H.; Zhou, J.; Jia, D.; Zhou, Y. Room-temperature multiferroic and magnetodielectric properties of SrTiO<sub>3</sub>/NiFe<sub>2</sub>O<sub>4</sub> composite ceramics. *Ceram. Int.* **2019**, *45*, 8238–8242. [[CrossRef](#)]
14. Jian, G.; Xue, F.; Zhang, C.; Yan, C.; Zhao, N.; Wong, C.P. Orientation dependence of elastic and piezomagnetic properties in NiFe<sub>2</sub>O<sub>4</sub>. *J. Magn. Magn. Mater.* **2017**, *442*, 141–144. [[CrossRef](#)]
15. Dey, P.; Debnath, R.; Singh, S.; Mandal, S.K.; Roy, J.N. Irreversibility in room temperature current–voltage characteristics of NiFe<sub>2</sub>O<sub>4</sub> nanoparticles: A signature of electrical memory effect. *J. Magn. Magn. Mater.* **2017**, *421*, 132–137. [[CrossRef](#)]
16. Jin, R.; Jiang, H.; Sun, Y.; Ma, Y.; Li, H.; Chen, G. Fabrication of NiFe<sub>2</sub>O<sub>4</sub>/C hollow spheres constructed by mesoporous nanospheres for high-performance lithium-ion batteries. *Chem. Eng. J.* **2016**, *303*, 501–510. [[CrossRef](#)]
17. Xu, R.; Huang, J.; Barnard, E.S.; Hong, S.S.; Singh, P.; Wong, E.K.; Jansen, T.; Harbola, V.; Xiao, J.; Wang, B.Y. Strain-induced room-temperature ferroelectricity in SrTiO<sub>3</sub> membranes. *Nat. Commun.* **2020**, *11*, 1–8.
18. He, J.; Lu, X.; Zhu, W.; Hou, Y.; Ti, R.; Huang, F.; Lu, X.; Xu, T.; Su, J.; Zhu, J. Induction and control of room-temperature ferromagnetism in dilute Fe-doped SrTiO<sub>3</sub> ceramics. *Appl. Phys. Lett.* **2015**, *107*, 12409. [[CrossRef](#)]
19. Zhang, W.; Li, H.-P.; Pan, W. Ferromagnetism in electrospun Co-doped SrTiO<sub>3</sub> nanofibers. *J. Mater. Sci.* **2012**, *47*, 8216–8222. [[CrossRef](#)]
20. Zhu, H.-Y.; Jiang, R.; Fu, Y.-Q.; Li, R.-R.; Yao, J.; Jiang, S.-T. Novel multifunctional NiFe<sub>2</sub>O<sub>4</sub>/ZnO hybrids for dye removal by adsorption, photocatalysis and magnetic separation. *Appl. Surf. Sci.* **2016**, *369*, 1–10. [[CrossRef](#)]
21. Gorgizadeh, M.; Azarpira, N.; Sattarahmady, N. In vitro and in vivo tumor annihilation by near-infrared photothermal effect of a NiFe<sub>2</sub>O<sub>4</sub>/C nanocomposite. *Colloids Surf. B Biointerfaces* **2018**, *170*, 393–400. [[CrossRef](#)]
22. Rodrigues, A.R.O.; Rio, I.S.R.; Coutinho, E.M.S.; Coutinho, P.J.G. Development of NiFe<sub>2</sub>O<sub>4</sub>/Au nanoparticles covered with lipid bilayers for applications in combined cancer therapy. In Proceedings of the Fourth International Conference on Applications of Optics and Photonics, Lisbon, Portuga, 31 May–4 June 2019; Volume 11207, p. 1120710.
23. Cabral, T.C.S.; Ardisson, J.D.; de Miranda, M.C.; Gomes, D.A.; Fernandez-Outon, L.E.; Sousa, E.M.B.; Ferreira, T.H. Boron nitride nanotube@NiFe<sub>2</sub>O<sub>4</sub>: A highly efficient system for magnetohyperthermia therapy. *Nanomedicine* **2019**, *14*, 3075–3088. [[CrossRef](#)]
24. Zhang, Y.; Xie, M.; Roscow, J.; Bao, Y.; Zhou, K.; Zhang, D.; Bowen, C.R. Enhanced pyroelectric and piezoelectric properties of PZT with aligned porosity for energy harvesting applications. *J. Mater. Chem. A* **2017**, *5*, 6569–6580. [[CrossRef](#)] [[PubMed](#)]
25. Roscow, J.I.; Lewis, R.W.C.; Taylor, J.; Bowen, C.R. Modelling and fabrication of porous sandwich layer barium titanate with improved piezoelectric energy harvesting figures of merit. *Acta Mater.* **2017**, *128*, 207–217. [[CrossRef](#)]
26. Castro, A.; Morère, J.; Cabañas, A.; Ferreira, L.P.; Godinho, M.; Ferreira, P.; Vilarinho, P.M. Designing nanocomposites using supercritical CO<sub>2</sub> to insert Ni nanoparticles into the pores of nanopatterned BaTiO<sub>3</sub> thin films. *J. Mater. Chem. C* **2017**, *5*, 1083–1089. [[CrossRef](#)]

27. Castro, A.; Martins, M.A.; Ferreira, L.P.; Godinho, M.; Vilarinho, P.M.; Ferreira, P. Multifunctional nanopatterned porous bismuth ferrite thin films. *J. Mater. Chem. C* **2019**, *7*, 7788–7797. [[CrossRef](#)]
28. Baumgartner, J.; Dey, A.; Bomans, P.H.H.; Le Coadou, C.; Fratzl, P.; Sommerdijk, N.A.J.M.; Faivre, D. Nucleation and growth of magnetite from solution. *Nat. Mater.* **2013**, *12*, 310–314. [[CrossRef](#)]
29. Deshpande, K.; Mukasyan, A.; Varma, A. Direct synthesis of iron oxide nanopowders by the combustion approach: Reaction mechanism and properties. *Chem. Mater.* **2004**, *16*, 4896–4904. [[CrossRef](#)]
30. George, C.N.; Thomas, J.K.; Jose, R.; Kumar, H.P.; Suresh, M.K.; Kumar, V.R.; Wariar, P.R.S.; Koshy, J. Synthesis and characterization of nanocrystalline strontium titanate through a modified combustion method and its sintering and dielectric properties. *J. Alloys Compd.* **2009**, *486*, 711–715. [[CrossRef](#)]
31. Leventis, N.; Chandrasekaran, N.; Sadekar, A.G.; Sotiriou-Leventis, C.; Lu, H. One-pot synthesis of interpenetrating inorganic/organic networks of CuO/resorcinol-formaldehyde aerogels: Nanostructured energetic materials. *J. Am. Chem. Soc.* **2009**, *131*, 4576–4577. [[CrossRef](#)]
32. Brun, N.; García-González, C.A.; Smirnova, I.; Titirici, M.M. Hydrothermal synthesis of highly porous carbon monoliths from carbohydrates and phloroglucinol. *RSC Adv.* **2013**, *3*, 17088–17096. [[CrossRef](#)]
33. Zhang, X.; Han, D.; Hua, Z.; Yang, S. Porous Fe<sub>3</sub>O<sub>4</sub> and gamma-Fe<sub>2</sub>O<sub>3</sub> foams synthesized in air by sol-gel autocombustion. *J. Alloys Compd.* **2016**, *684*, 120–124. [[CrossRef](#)]
34. Xia, Y.; He, Z.; Lu, Y.; Tang, B.; Sun, S.; Su, J.; Li, X. Fabrication and photocatalytic property of magnetic SrTiO<sub>3</sub>/NiFe<sub>2</sub>O<sub>4</sub> heterojunction nanocomposites. *RSC Adv.* **2018**, *8*, 5441–5450. [[CrossRef](#)]
35. Kočí, K.; Obalová, L.; Matějová, L.; Plachá, D.; Lacný, Z.; Jirkovský, J.; Šolcová, O. Effect of TiO<sub>2</sub> particle size on the photocatalytic reduction of CO<sub>2</sub>. *Appl. Catal. B Environ.* **2009**, *89*, 494–502. [[CrossRef](#)]
36. Viennois, R.; Hermet, P.; Machon, D.; Koza, M.M.; Bourgogne, D.; Fraisse, B.; Petrović, A.P.; Maurin, D. Stability and Lattice Dynamics of Ruddlesden–Popper Tetragonal Sr<sub>2</sub>TiO<sub>4</sub>. *J. Phys. Chem. C* **2020**, *124*, 27882–27893. [[CrossRef](#)]
37. Ge, W.; Zhu, C.; An, H.; Li, Z.; Tang, G.; Hou, D. Sol-gel synthesis and dielectric properties of Ruddlesden–Popper phase Sr<sub>n+1</sub>Ti<sub>n</sub>O<sub>3n+1</sub> (n = 1, 2, 3, ∞). *Ceram. Int.* **2014**, *40*, 1569–1574. [[CrossRef](#)]
38. Luque, R.; Campelo, J.M.; Luna, D.; Marinas, J.M.; Romero, A.A. Catalytic performance of Al-MCM-41 materials in the N-alkylation of aniline. *J. Mol. Catal. A Chem.* **2007**, *269*, 190–196. [[CrossRef](#)]
39. Kruk, M.; Jaroniec, M. Gas adsorption characterization of ordered organic–inorganic nanocomposite materials. *Chem. Mater.* **2001**, *13*, 3169–3183. [[CrossRef](#)]
40. Walerczyk, W.; Zawadzki, M.; Grabowska, H. Solvothermal Synthesis and Catalytic Properties of Nanocrystalline ZnFe<sub>2–x</sub>Al<sub>x</sub>O<sub>4</sub> (x = 0, 1, 2) Spinel in Aniline Methylation. *Catal. Letters* **2012**, *142*, 71–80. [[CrossRef](#)]
41. Li, Y.; Zhou, X.; Luo, W.; Cheng, X.; Zhu, Y.; El-Toni, A.M.; Khan, A.; Deng, Y.; Zhao, D. Pore Engineering of Mesoporous Tungsten Oxides for Ultrasensitive Gas Sensing. *Adv. Mater. Interfaces* **2019**, *6*(1), 1801269. [[CrossRef](#)]
42. Han, S.; Hyeon, T. Simple silica-particle template synthesis of mesoporous carbons. *Chem. Commun.* **1999**, *19*, 1955–1956. [[CrossRef](#)]
43. Kushwaha, S.; Sreelatha, G.; Padmaja, P. Physical and chemical modified forms of palm shell: Preparation, characterization and preliminary assessment as adsorbents. *J. Porous Mater.* **2013**, *20*, 21–36. [[CrossRef](#)]
44. Zeng, K.; Zhang, D. Recent progress in alkaline water electrolysis for hydrogen production and applications. *Prog. Energy Combust. Sci.* **2010**, *36*, 307–326. [[CrossRef](#)]
45. Borhan, A.I.; Gherca, D.; Cojocaru, Ș.; Lupu, N.; Roman, T.; Zaharia, M.; Palamaru, M.N.; Iordan, A.R. One-pot synthesis of hierarchical magnetic porous γ-Fe<sub>2</sub>O<sub>3</sub>@NiFe<sub>2</sub>O<sub>4</sub> composite with solid-phase morphology changes promoted by adsorption of anionic azo-dye. *Mater. Res. Bull.* **2020**, *122*, 110664. [[CrossRef](#)]
46. Yu, Z.; Ang, C. Maxwell–Wagner polarization in ceramic composites BaTiO<sub>3</sub>–(Ni<sub>0.3</sub>Zn<sub>0.7</sub>)Fe<sub>2.1</sub>O<sub>4</sub>. *J. Appl. Phys.* **2002**, *91*, 794–797. [[CrossRef](#)]
47. Zeng, F.; Cao, M.; Zhang, L.; Liu, M.; Hao, H.; Yao, Z.; Liu, H. Microstructure and dielectric properties of SrTiO<sub>3</sub> ceramics by controlled growth of silica shells on SrTiO<sub>3</sub> nanoparticles. *Ceram. Int.* **2017**, *43*, 7710–7716. [[CrossRef](#)]
48. Jonscher, A.K. *Dielectric Relaxation in Solids*; Chelsea Dielectrics Press Limited: London, UK, 1983.
49. Li, G.; Liu, H.; Wang, Z.; Hao, H.; Yao, Z.; Cao, M.; Yu, Z. Dielectric properties and relaxation behavior of Sm substituted SrTiO<sub>3</sub> ceramics. *J. Mater. Sci. Mater. Electron.* **2014**, *25*, 4418–4424. [[CrossRef](#)]
50. Lu, S.G.; Xu, Z.K.; Wang, Y.P.; Guo, S.S.; Chen, H.; Li, T.L.; Or, S.W. Effect of CoFe<sub>2</sub>O<sub>4</sub> content on the dielectric and magnetoelectric properties in Pb(ZrTi)O<sub>3</sub>/CoFe<sub>2</sub>O<sub>4</sub> composite. *J. Electroceramics* **2008**, *21*, 398. [[CrossRef](#)]
51. Bammannavar, B.K.; Naik, L.R. Electrical properties and magnetoelectric effect in (x) Ni<sub>0.5</sub>Zn<sub>0.5</sub>Fe<sub>2</sub>O<sub>4</sub><sup>4+(1-x)</sup> BPZT composites. *Smart Mater. Struct.* **2009**, *18*, 085013. [[CrossRef](#)]
52. Pei, Y.; Li, Q.; Shi, W.; Zhang, B.; Chen, Q.; Yue, X.; Xiao, D.; Zhu, J. Effect of CoFe<sub>2</sub>O<sub>4</sub> content on the dielectric and magnetoelectric properties in CoFe<sub>2</sub>O<sub>4</sub>/Pb(Mg<sub>1/3</sub>Nb<sub>2/3</sub>)<sub>0.35</sub>Ti<sub>0.65</sub>O<sub>3</sub> composites. *Ferroelectrics* **2010**, *410*, 82–87. [[CrossRef](#)]